

## The Lunar Orbiter Laser Altimeter Investigation on the Lunar Reconnaissance Orbiter Mission

David E. Smith · Maria T. Zuber · Glenn B. Jackson · John F. Cavanaugh · Gregory A. Neumann · Haris Riris · Xiaoli Sun · Ronald S. Zellar · Craig Coltharp · Joseph Connelly · Richard B. Katz · Igor Kleyner · Peter Liiva · Adam Matuszeski · Erwan M. Mazarico · Jan F. McGarry · Anne-Marie Novo-Gradac · Melanie N. Ott · Carlton Peters · Luis A. Ramos-Izquierdo · Lawrence Ramsey · David D. Rowlands · Stephen Schmidt · V. Stanley Scott III · George B. Shaw · James C. Smith · Joseph-Paul Swinski · Mark H. Torrence · Glenn Unger · Anthony W. Yu · Thomas W. Zagwodzki

Received: 5 January 2009 / Accepted: 15 April 2009 / Published online: 16 May 2009  
© Springer Science+Business Media B.V. 2009

**Abstract** The Lunar Orbiter Laser Altimeter (LOLA) is an instrument on the payload of NASA's Lunar Reconnaissance Orbiter spacecraft (LRO) (Chin et al., in Space Sci. Rev. 129:391–419, 2007). The instrument is designed to measure the shape of the Moon by measuring precisely the range from the spacecraft to the lunar surface, and incorporating precision orbit determination of LRO, referencing surface ranges to the Moon's center of mass. LOLA has 5 beams and operates at 28 Hz, with a nominal accuracy of 10 cm. Its primary objective is to produce a global geodetic grid for the Moon to which all other observations can be precisely referenced.

**Keywords** Moon · Shape · Space instrumentation · Topography

---

D.E. Smith · G.A. Neumann · H. Riris · X. Sun · E.M. Mazarico · J.F. McGarry · D.D. Rowlands · V.S. Scott III · J.-P. Swinski · T.W. Zagwodzki  
Solar System Exploration Division, NASA Goddard Space Flight Center, Greenbelt, MD 20771, USA

M.T. Zuber (✉)  
Department of Earth, Atmospheric and Planetary Sciences, Massachusetts Institute of Technology,  
Cambridge, MA 02139-4307, USA  
e-mail: [zuber@mit.edu](mailto:zuber@mit.edu)

G.B. Jackson · J.F. Cavanaugh · R.S. Zellar · C. Coltharp · J. Connelly · R.B. Katz · I. Kleyner · A. Matuszeski · A.-M. Novo-Gradac · M.N. Ott · C. Peters · L.A. Ramos-Izquierdo · L. Ramsey · S. Schmidt · G.B. Shaw · J.C. Smith · G. Unger · A.W. Yu  
Advanced Engineering Technology Directorate, NASA Goddard Space Flight Center, Greenbelt, MD 20771, USA

M.H. Torrence  
Stinger Ghaffarian Technologies, Greenbelt, MD 20770, USA

P. Liiva  
Sigma Space Corporation, Lanham, MD 20706, USA

## 1 Introduction

The Lunar Orbiter Laser Altimeter (LOLA) is an instrument designed to assist in the selection of landing sites on the Moon for future robotic and human exploration. The primary motivation is that any future mission proposed to land on the surface of the Moon would need to be certain from the best available information that the location would be safe for robotic and/or human endeavors. In this context, LOLA was proposed for the payload of the Lunar Reconnaissance Orbiter (LRO) mission (Chin et al. 2007) to provide the geodetic location, the direction and magnitude of surface slopes, and the elevation variation at scales relevant to landing and surface mobility, the latter generally referred to as surface roughness. In addition, since one of the objectives of NASA's Exploration Program is to attempt to detect the presence of water ice on or near the surface, LOLA was designed to measure surface reflectance at the laser wavelength as any significant water ice crystals on the lunar surface would provide a measurable increase in reflectance.

The present knowledge of the topography of the Moon (cf. Wieczorek 2007) is not adequate for ensuring a safe landing in any but a few locations, such as those visited by the Apollo flights. Based on all previous missions to the Moon, knowledge of the position of features on the surface is at approximately the kilometer level and in many areas, such as the lunar far side, that knowledge is of order many kilometers. In addition, the slope of the surface at the majority of locations is completely unknown on scales of 10's to 100's of kilometers. For topography, and more generally for the shape of the Moon, the major source of data for the last 15 years has been the Clementine mission (Nozette et al. 1994), launched in 1994, which carried a laser altimeter that provided the first near-global topographic mapping of the Moon (Smith et al. 1997; Zuber et al. 1994); the exception being the regions within about 10 to 15 degrees of each pole. Clementine provided 100-m quality radial information and similar horizontal quality position information with a spatial resolution of order 1 degree ( $\sim 30$  km) at the equator. The lunar shape measured by Clementine is shown in Fig. 1 (Zuber et al. 1994). A more recent effort combined Clementine altimetry (Smith et al. 1997) with elevation models of the lunar polar regions from stereo-photogrammetry (e.g. Cook et al. 2000). This model (U.S. Geological Survey 2002) has improved spatial resolution at the poles but lacks geodetic control.

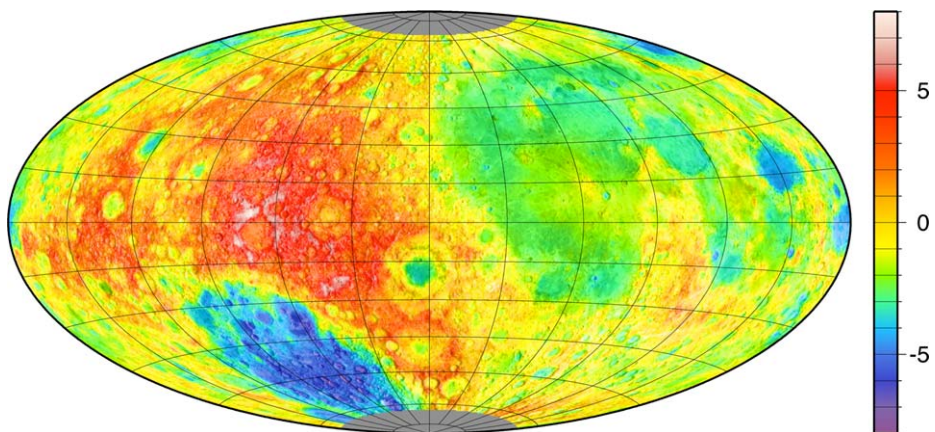


**Fig. 1** Clementine lunar topography (Smith et al. 1997). Clementine altimetry data did not extend to the poles; estimated overall radial accuracy is 100 m. The topography scale is in kilometers

A new USGS Unified Lunar Control Network (ULCN 2005) based upon most available data was released in 2006 (Archinal et al. 2006).

Recently, laser altimeters have flown to the Moon on missions from the Chinese, Japanese and Indian space agencies. The Chinese (Qian 2008) and Japanese (Araki et al. 2009) instruments, both single-beam 1-Hz ranging systems, operated successfully in lunar orbit. The Indian instrument (Kamalakar et al. 2005), a single-beam 10-Hz ranging system similar to MOLA at Mars (Smith et al. 1999; Zuber et al. 1992), began mapping in fall 2008. While so far the Chinese and Japanese instruments have improved lunar topographic knowledge, their reported range accuracy of 5 to 10 m, and measurement spacing along track of 150 m to 1.5 km dictate that none of these systems meet the requirements identified by the NASA Exploration Program, which included 30-m along-track measurement spacing, meter-level ranging, and surface roughness and slope measurements.

In order to improve significantly our knowledge of the lunar topography, it was necessary employ a greater accuracy altimetric ranging system and be able to determine the position of the LRO spacecraft to significantly greater accuracy than had been achieved on earlier missions. In addition, the spacecraft altitude and the timing of the observations would be needed to commensurate accuracy.

## 2 Investigation Description

### 2.1 Exploration

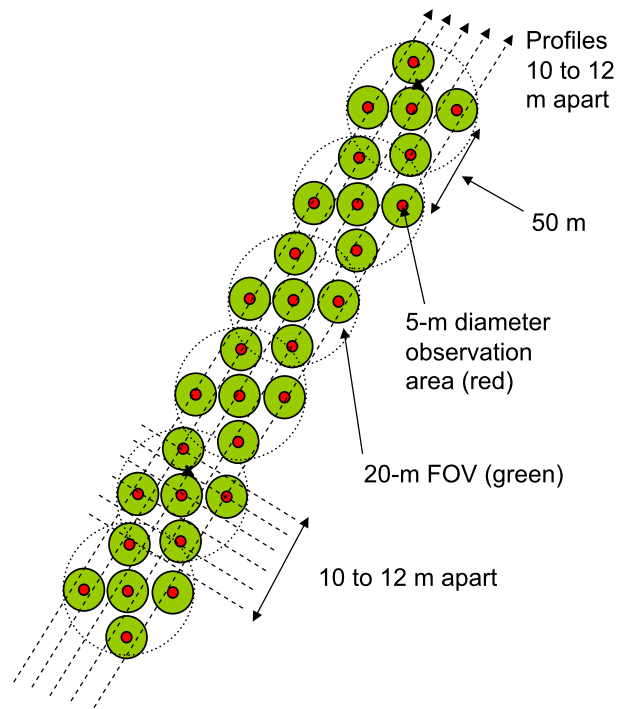
The LOLA investigation is designed to assist in the selection of future landing sites by providing topographic, surface roughness, surface slope, and surface reflectance measurements, and a global lunar coordinate system that provides information on the positions of lunar surface features. In the design and development of the instrument, certain assumptions were made about the geodetic requirements for landing on the lunar surface, particularly spatial resolution and positional accuracy. The assumptions used to guide the instrument design are shown in Table 1. These assumptions are in three categories: landing site knowledge, instrument performance, and spacecraft positional and orbital knowledge.

In order for positional accuracies to be achieved globally, it is necessary to develop an improved lunar reference system or grid that has an internal consistency at the ~50-m level. This grid could then be compared with the known positions of the Apollo landing sites so that all LRO and previous lunar data could be incorporated into the LRO/LOLA-derived

**Table 1** Assumptions in LOLA instrument investigation that guided design of the system and were not being met by other lunar laser altimeters

Lander scale	~5 m	Approx. size of Apollo landed module
Landing area	~50 to 100 m	
Slope accuracy in 2 directions	$\pm 1^\circ$ , 10-m baseline	
Elevation precision	$\pm 0.1$ m	
Radial accuracy	<1 m	Includes orbit and instrumental errors
Horizontal accuracy	<50 m	Landing site size
Surface roughness	0.3 m	Typical height clearance of Mars lander
Spacecraft position	H: 50 m; V: <1 m	Landing site positional knowledge
Spacecraft timing	3 ms	Spacecraft velocity is ~1.6 m/s

**Fig. 2** LOLA's five laser spot pattern on the lunar surface

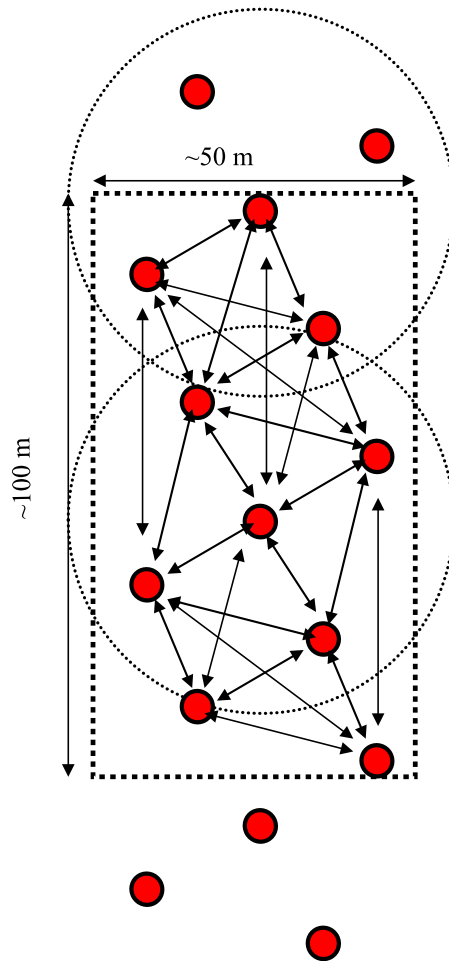


coordinate frame. The development of an accurate ( $\sim 50$ -m) global geodetic grid was considered to be the highest priority objective of the LOLA investigation and will ultimately provide the control at regional and local scales. An internal consistency at the 50-m level also requires spatial positioning of the LRO spacecraft of similar quality, which in itself requires improvements be made to the lunar gravity model. This improvement is expected to come from the global coverage of laser altimeter data in combination with tracking of the LRO spacecraft. Nominal LRO tracking is by the Universal Space Network (USN) at S-band with approximately  $\pm 1$  mm/s Doppler per 10 s augmented by laser ranging (LR) (Zuber et al. 2009), which is able to provide approximately  $\pm 10$  cm range measurements at 28 Hz.

The determination of the full surface slope requires the measurement of slope in two directions and hence the altimeter must make measurements across track as well as along track. This requirement is accomplished in LOLA by a multi-beam approach that provides 5 measurements in an X-pattern from which the slopes along track and across track can be derived on scales of approximately 25 m. This X-formation also has the advantage that, suitably rotated, will provide, 5 near-equidistant parallel profiles spaced at approximately 12 m. Figure 2 shows the 5-spot pattern on the lunar surface that LOLA will implement.

The 5 parallel profiles, providing 5 measurements of altitude, surface roughness, and surface brightness for each laser pulse, characterize a continuous strip of the lunar surface 50- to 60-m wide and will provide an assessment of the suitability of the area as a “lunar landing strip”. Graphical displays of the data from LOLA, provided within hours of the data being returned will show the elevation of the surface, an estimate of the surface roughness and surface reflectance, and the derived measurements of the slope of the surface. Figure 3 shows the large number of slopes on various baselines derivable from 10 observations obtainable in less than 0.1 seconds of operation.

**Fig. 3** Surface slope measurements from LOLA profiles showing along and across-track capability on baselines of 25 m to 50 m



The surface reflectance represents a measure of the albedo of the surface at the laser wavelength of 1064 nm and its measurement has been designed into the instrument with the aim of being able to detect the presence of surface ice at small areal density. The measurement is accomplished by estimating the energy of the return laser signal and comparing it with the output energy. Note that this measurement is calibrated in a relative sense, with respect to pre-launch testing, as the instrument lacks a source with known brightness in flight. Nonetheless, experience has shown the measurement to be extremely stable based on experience in ranging at Mars (Smith et al. 2001; Sun et al. 2001). The brightness of ice crystals on the lunar surface is expected to have an albedo of  $>0.8$  (Abshire et al. 2005), and is approximately 4 times the average albedo ( $\sim 0.2$ ) of the regolith. Thus an albedo measurement of 10 to 15% in each of the 5-m spots on the lunar surface would enable ice crystal areal densities of 4 or 5% to be detected. The possible detection of surface ice by LOLA, although not the instrument's prime measurement, is considered a potential high-priority opportunity to address one of LRO's primary mission objectives.

The resolution across track depends on the number of orbits of the spacecraft. After one year the across-track resolution is approximately  $0.04^\circ$ , providing an average separation of



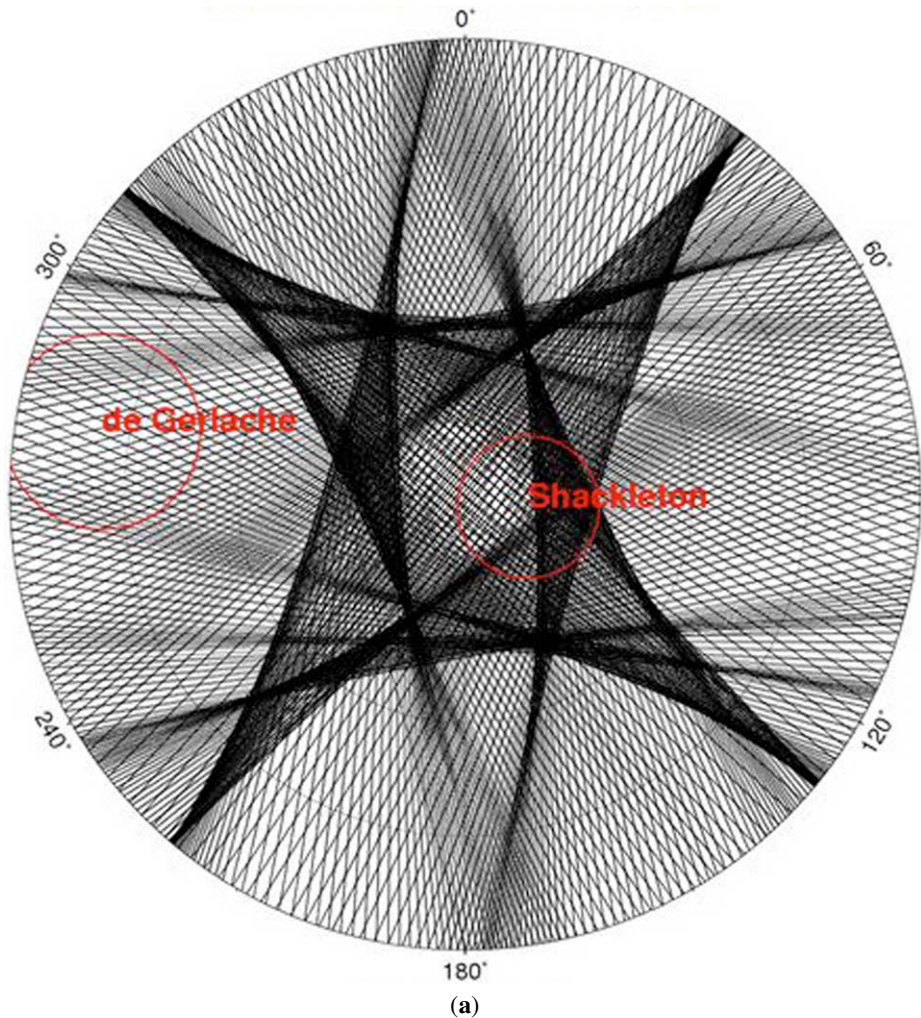


**Fig. 4** (a) Example of south polar coverage, lat  $88^{\circ}\text{S}$  to the pole. (b) Example of coverage lat  $80^{\circ}\text{S}$  to the pole showing the range of spacecraft heights. The height scale is in kilometers

the LOLA swaths at the equator of order 1.2 km, and at latitudes  $80^{\circ}\text{N}$  and  $\text{S}$  a separation of order 200 m. Figures 4a and 4b show the coverage from  $88^{\circ}\text{S}$  to the pole for a typical month and  $80^{\circ}\text{S}$  to the pole; each month is very similar to the next although the ground tracks do not repeat.

## 2.2 Science

In addition to providing measurements for exploration, the LOLA Investigation Team will also conduct a variety of scientific studies to address a wide variety of outstanding questions in lunar science.

(a) LOLA will improve the current understanding of impact flux on the Moon, especially during its early history, by helping to identify and characterize topographic expressions of

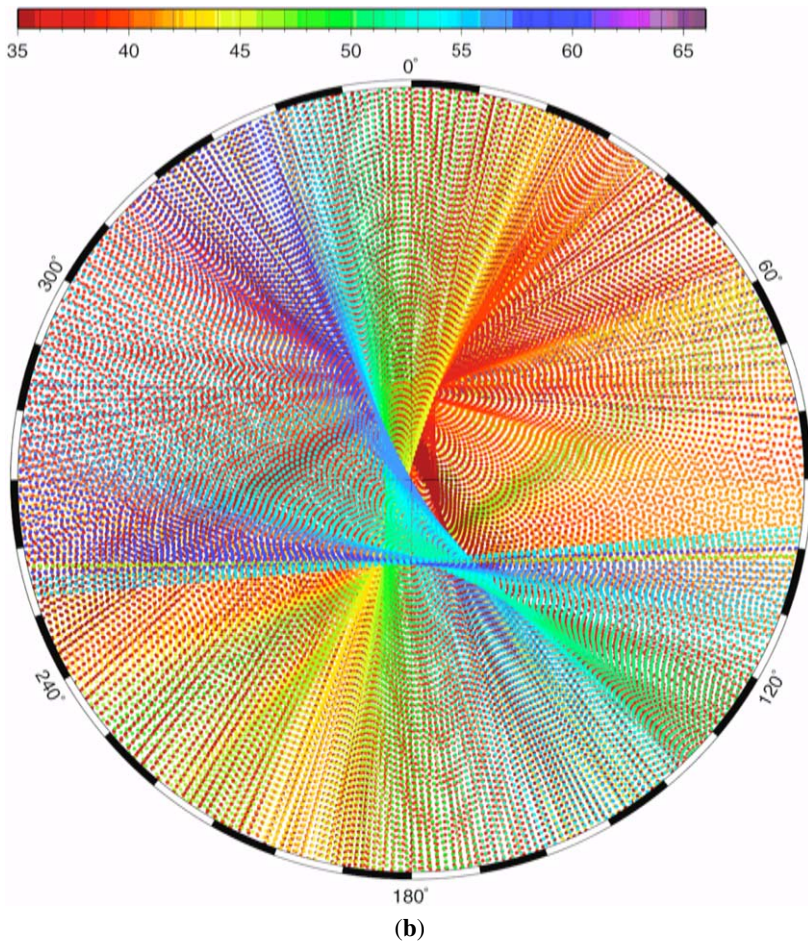


**Fig. 4** (Continued)

crater-like circular structures otherwise undetectable in visible images (Frey et al. 2002). Their size-frequency distribution will provide new constraints on the cratering history subsequent to the late heavy bombardment. In addition, LOLA will provide greater insights on the factors that contribute to the formation of craters, including improvements to the connection between an observed crater and the projectile size/impact velocity which generated it (cf. Melosh 1989), yielding an improved understanding of the size-frequency distribution of the primary impactor population striking the Moon (Hartmann 1970).

(b) Topography and gravity are fundamental measurements that provide information on the lunar interior structure. LOLA topography in combination with high-resolution gravity soon to be available from the Gravity Recovery and Interior Laboratory (GRAIL) mission (Zuber et al. 2008a) will be used to map the Moon's global crustal and lithosphere thickness as well as crustal and mantle density anomalies. These observations will be applied, *inter alia*, to study the structure of impact basins as a measure of the influence of impactors on the shallow interior of the Moon.

Models of the planetary interior depend explicitly on the estimate of the polar moment of inertia, which measures the radial distribution of mass. The  $k_2$  Love number of the Moon, which measures the tidal response of the potential, has been determined from analysis of satellite tracking data (e.g., Konopliv et al. 2001), with  $k_2 = 0.026 \pm 0.003$  (Goossens and Matsumoto 2008), from a re-analysis of Lunar Prospector (LP) and historical data, found  $k_2 = 0.0213 \pm 0.0075$ . The LRO data, LOLA altimetry, S-band tracking, and LR ranging, will lead to an independent estimate of this important physical parameter. In addition, from altimetry and LRO laser ranging (LR) (Zuber et al. 2009), we will be able to estimate the global  $h_2$  Love number—which reflects the global geometric radial response of the Moon to tidal deformation and whose uncertainty is currently  $\sim 25\%$ .

(c) Lunar albedo measurements, independent of illumination conditions, can be made by LOLA. To characterize possible volatiles in permanently shadowed polar regions, LOLA provides a bidirectional reflectance (albedo) at zero phase angle by means of the ratio of transmitted and returned energy measurements, and is capable of revealing concentrations of a few percent of surface water ice (see Sect. 2.1).

(d) LOLA data will be used to make quantitative assessments of volcanic landforms and source regions, and the characterization of lava flows and their stratigraphic relationships. Magmatic intrusions (dikes and sills) result in unique patterns of uplift and deformation at the surface that can be used to invert for the geometry of the underlying magma bodies. LOLA topographic data will be used to discriminate between magmatic and non-magmatic tectonism, and to constrain the volumes of the underlying magma bodies. Similar analyses have been successfully applied to the study of dikes on the Earth and Mars (e.g., Schultz et al. 2004).

(e) Ridges and rilles are tectonic structures that reflect basin-scale loading processes (Quaide 1965). The high spatial and vertical resolution of LOLA data will allow significant improvements in the estimation of strain associated loading of maria units, and will improve understanding of both the thermomechanical state of the underlying lithosphere and the history of volcanic extrusion within major impact basins.

(f) LOLA data will be used to improve knowledge of impact cratering and the processes in shaping planetary crusts, particularly, early in their history (Melosh 1989). New information will be obtained at all scales including multi-ring basins (e.g., Hartmann 1971), which play a significant role in shaping the topography of the terrestrial planets (cf. Spudis et al. 1994). The topographic signature of basin ring structures on the Moon is presently poorly resolved in Clementine topography (Zuber et al. 1994). LOLA topography is expected to enable the first very high-resolution study of well-preserved multi-ring structures, thereby providing important information regarding their underlying structure and formation.

(g) Ejecta generated by impact processes constitute one of the primary sources of regolith and influences its subsequent evolution (Melosh 1989). High-resolution topographic analyses of ejecta at lunar craters using LOLA will provide new constraints on the thickness, run out, roughness, and block-size distributions of such ejecta as a function of crater and basin size (Soderblom 1970). These measurements will collectively provide a quantitative means to assess the role of ejecta in the formation and evolution of regolith.

In addition, many science objectives are enabled or supported by the knowledge of topography, roughness, and surface slopes, which depend on precision laser tracking and orbit determination of LRO. Thus, LOLA will re-analyze its data using the GRAIL gravity model that is expected in 2012 and thereby improve geodetic framework for all other lunar data. In addition, we plan to combine the Kaguya (Araki et al. 2009) and Chandrayaan (Kamalakar et al. 2005) altimetry with LRO data for an extended, fully compatible and inter-calibrated dataset. We will also combine data from LOLA and the Lunar Reconnaissance Orbiter Camera (LROC) (Robinson et al. 2009) in a joint LOLA/LROC activity, for



geodetically-controlled stereo topography to obtain the highest-resolution Digital Elevation Models (DEMs). The LOLA global data products, working with LROC (Robinson et al. 2009), will be cartographically-tied to the Lunar Laser Retro Reflectors (Dickey et al. 1994) and the Apollo and Lunakhod sites and thus incorporate the most precise lunar orientation/libration properties.

### 2.3 Orbit Determination for LOLA

The quality of the topographic measurements and models depends upon the quality of the altimeter and its supporting data, and also on the knowledge of the spacecraft orbit. The routine operational tracking data of LRO will be S-band Doppler acquired for approximately 20 hours per day and an accuracy of order 1 mm/s every 10 seconds ( $1\sigma$ ). The altimeter has decimeter accuracy but the orbital error is expected to be significantly larger. Orbits for LRO will be developed by the LOLA team using a combinations of the S-band Doppler and laser tracking (Zuber et al. 2009) in conjunction with the altimetry.

An important tool of the LOLA orbit determination activity is the altimeter used in the orbital crossover mode. At an orbital crossover the lunar radius is the same by definition, as is the surface roughness, and the implied surface slopes. The equivalence of these measurements at the same location on different orbits enables the location of the crossover to be determined and the altimeter measurements to be used as an observable in determining the orbit of LRO, and also for estimating other parameters, such as pointing and timing, and gravity coefficients of the lunar gravity field (Rowlands et al. 1999). In addition, the very precise laser ranging observations (Zuber et al. 2009) will constrain the LRO orbit to the decimeter level over the lunar near side and will significantly improve the orbit accuracy beyond that which will be achievable with S-band Doppler tracking alone, and also enable the estimation of additional force model parameters. At the conclusion of the analysis of all LOLA data and the simultaneous LRO orbit determination we expect the global radial positional accuracy at the 50-cm level and at the 25-m level in the horizontal. Further details on the crossover analysis are given in Zuber et al. (2009).

## 3 Instrument Design

### 3.1 Overview

The LOLA instrument configuration is shown in Fig. 5 and the key instrument parameters are shown in Table 2. LOLA uses a Q-switched Nd:YAG laser at 1064 nm and a silicon avalanche photodiode detector (SiAPD) to measure the time of flight (TOF) to the lunar surface from a nominal 50-km orbit. The transmitted laser beam is split in five different beams by a diffractive optical element (DOE), each beam having a 0.5-mrad spacing. The receiver telescope focuses the reflected beams into a fiber optic array, placed at the focal plane of the telescope. The array consists of five fibers and each fiber in the array is aligned with a laser spot on the ground. The fibers direct the reflected beams into five separate detectors. The detector electronics amplify the signal and time stamp the received pulses relative to the spacecraft mission elapsed time (MET) using a set of time-to-digital converters (TDC) with 0.5-ns resolution. The transmitted pulse is also time stamped and the TOF to the lunar surface can be determined. The LRO spacecraft carries an ultra-stable quartz oscillator and distributes the timing signal to LOLA and other instruments. A signal-processing algorithm running on an embedded processor continually adjusts the receiver gain and threshold levels

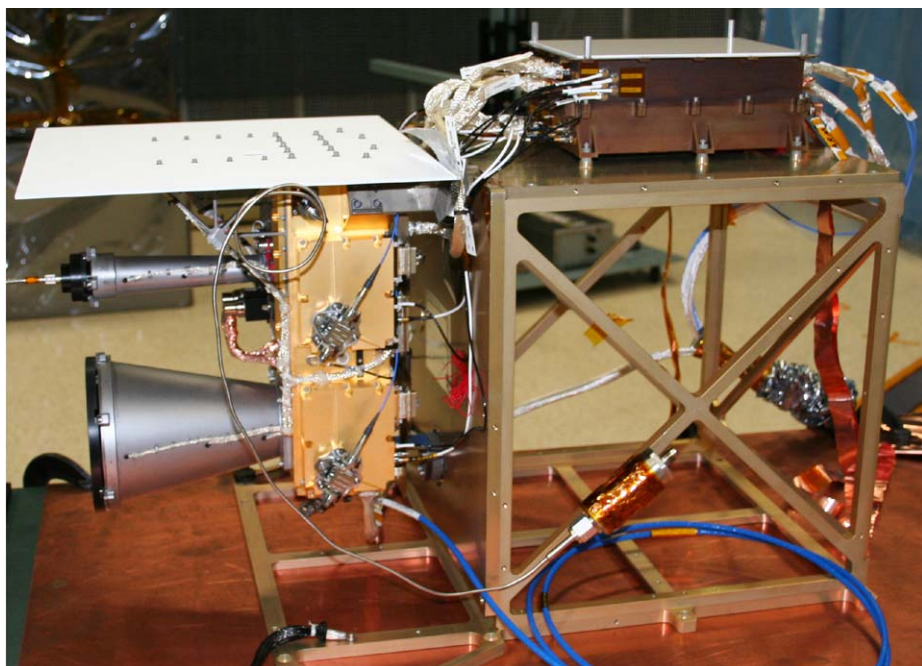


**Fig. 5** LOLA instrument configuration prior to thermal vacuum testing. The frame is a holding mechanism during the test. The electronic box is on the *top side of the frame*, the *white rectangle* is the radiator; the grey cone on the left is the receiver telescope; the laser beam expander is the small cone above the receiver telescope

**Table 2** Key LOLA instrument parameters

Parameter	Value
Laser wavelength	1064.4 nm
Pulse energy	2.7/3.2 mJ (laser1/laser2)
Pulse width	~5 ns
Pulse rate	$28 \pm 0.1$ Hz
Beam divergence	$100 \pm 10$ $\mu$ rad
Beam separation	$500 \pm 20$ $\mu$ rad
Receiver aperture diameter	0.14 m
Receiver field of view	$400 \pm 20$ $\mu$ rad
Receiver bandpass filter	0.8 nm
Detector responsivity (nominal)	300 kV/W
Detector active area diameter	0.7 mm
Detector electrical bandwidth	$46 \pm 5$ MHz
Timing resolution	0.5 ns

and maintains the range window centered on the lunar surface return. A functional block diagram of LOLA is shown in Fig. 6.

The LRO spacecraft also carries a unique laser ranging (LR) system (Zuber et al. 2009) for precise orbit determination. The laser ranging system consists of a 30-mm aperture op-

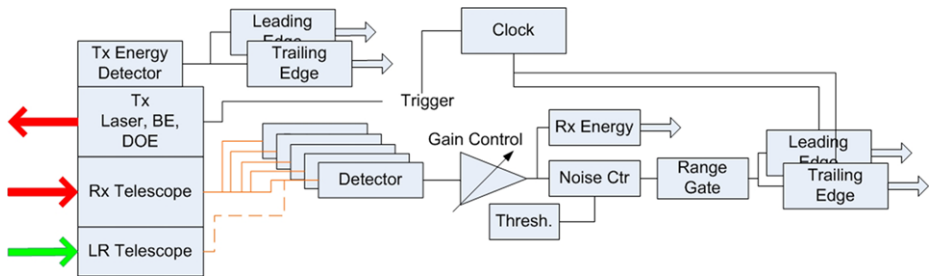


**Fig. 6** LOLA functional block diagram

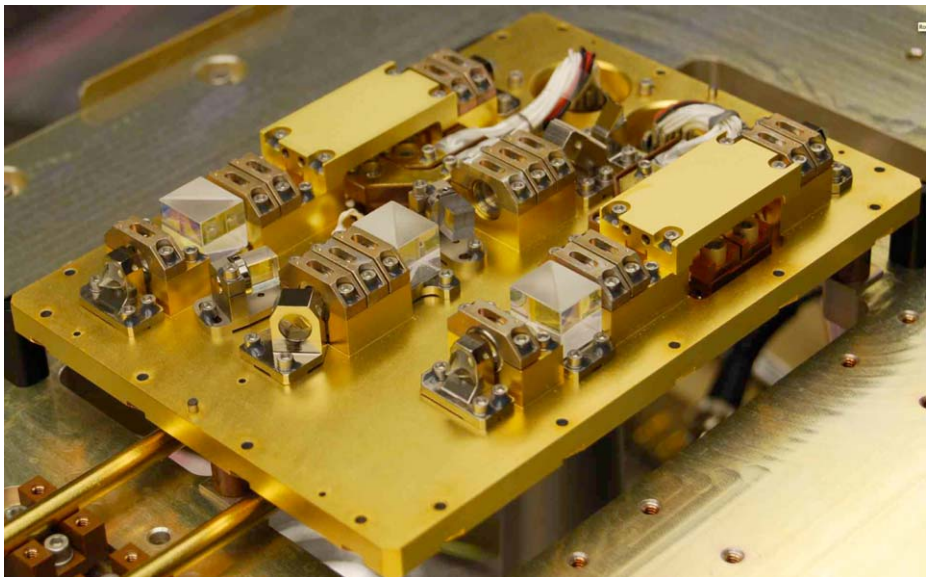


**Fig. 7** Laser transmitter showing two lasers

tical receiver mounted on the LRO spacecraft high gain antenna used for communications and data transmission. The ranging precision of the LR is nominally 10 cm at 28 Hz. The receiver is pointed to a ground (Earth) based laser satellite ranging station that sends a 532-nm laser pulse to LRO. The receiver focuses the incoming 532-nm beam into a fiber bundle and the laser pulses are then directed onto one of the five LOLA detectors modified to accommodate both signals at both 532 and 1064 nm. The combination of LOLA altimetry and LR on the lunar near side is expected to provide the position of LRO at the decimeter level and constrain the orbit of LRO on the near side in the orbit determination process. The LR system is described in a companion paper (Zuber et al. 2009).

### 3.2 LOLA Transmitter

The LOLA transmitter consists of two virtually identical, diode pumped, Q-switched Nd:YAG oscillators operating at 1064.4 nm (Fig. 7). The diode pump lasers are derated to increase their lifetime. The laser beams are combined with polarizing optics and only one

laser is operating at a time; the other one is redundant. The laser repetition rate is  $28 \pm 0.1$  Hz, the energy per pulse is  $\sim 2.7$  mJ for Laser 1 and  $\sim 3.0$  mJ for Laser 2. The pulse width is approximately 5 ns. The output of the laser is directed through an  $\times 18$  beam expander and then through the DOE to produce five beams separated by  $500 \pm 20$   $\mu$ rad. The laser beam prior to the beam expander has a divergence of 1.8 mrad. After the beam expander and DOE, each beam has a  $100 \pm 10$   $\mu$ rad divergence and approximately the same energy; some variation in the energy between beams is discernible due to imperfections in the DOE. The LOLA laser is designed to operate in vacuum but a significant amount of the subsystem and system testing was done in air. The laser cavity was integrated in a clean room and two filters in the laser housing are designed to prevent particulate and molecular contamination of the lasers prior to launch.

The laser beam pattern is rotated  $26^\circ$  relative to the spacecraft velocity vector. From the nominal orbit of 50 km, each laser spot is  $\sim 5$  m in diameter on the ground. The five-spot pattern will allow LOLA to measure both the slope and roughness of the lunar surface. The five beam spot pattern on the ground (including the field of view) relative to the spacecraft velocity vector is shown in Fig. 2.

A small kick-off mirror placed inside the laser box directs a small fraction of the laser power onto the SiAPD. The detector monitors the energy of the transmitted laser pulse and it also used as a fire acquisition signal that turns off the drive to the pump diode lasers. In addition, the outgoing pulse is time tagged and provides timing information for the time of flight measurement.

**Pulse width** LOLA monitors the laser-pulse energy and the pulsewidth at threshold crossing, which may be used to infer the transmitted laser-pulse shape. Note that the pulse shape output from the LOLA SPOT 4 detector is the convolution of the actual pulse shape and the impulse response of the transmit energy monitor. The relationship between the LOLA measured pulse width and the threshold value for Laser 1 and 2 was measured and the result is given in Fig. 10. The nominal transmit threshold setting is 116 mV. The average transmitted laser pulse energy is not expected to decrease significantly over the mission lifetime, thus the threshold value for the transmitted pulse should not have to be adjusted. If the laser or the transmitter common optics were to degrade, the threshold could be lowered to continue detecting transmitted laser pulses. There is approximately a factor of six adjustment that can be made on the transmit threshold (from 116 to 19 mV).

**Life Testing of Transmitter** As part of the development of the transmitter, a parallel life test program was conducted in order to verify the basic design, identify areas requiring modification, and provide an estimate of the lifetime that can be expected on orbit. This was particularly important for LOLA because of the use of a double transmitter system that would enable extended life of the instrument. The goal of the instrument was to acquire 1 billion pulses from each laser thus providing approximately 9 billion altimetric, pulse spreading and surface albedo measurements.

Three life tests at various stages were conducted. The first was on an early design that operated continuously for approximately 560 million shots that verified the basic design. The second test on a pre-engineering model (pre-EM) of the Laser 1 operated for approximately 520 million shots, and test 3 (presently in process) on an EM of Laser 2, has accumulated over 500 million shots without degradation. The requirement of the LRO mission for exploration is approximately 880 million total shots.

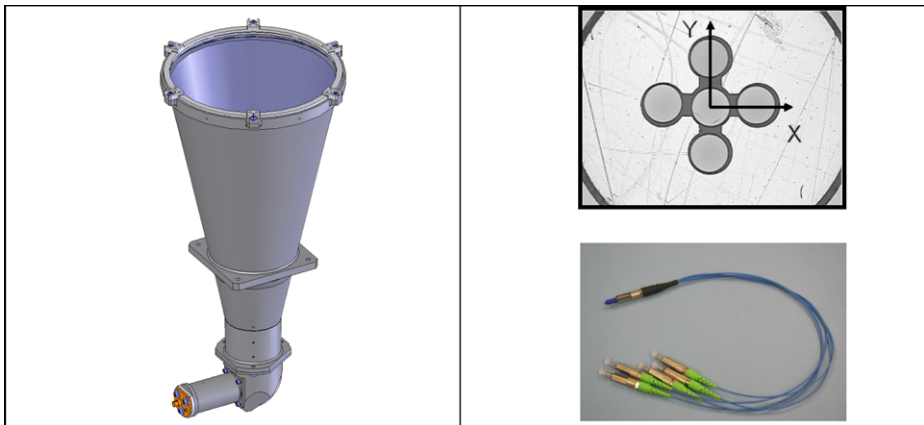


**Fig. 8** Receiver and fiber bundle. The fiber bundle takes the photons from the receiver telescope to the detectors

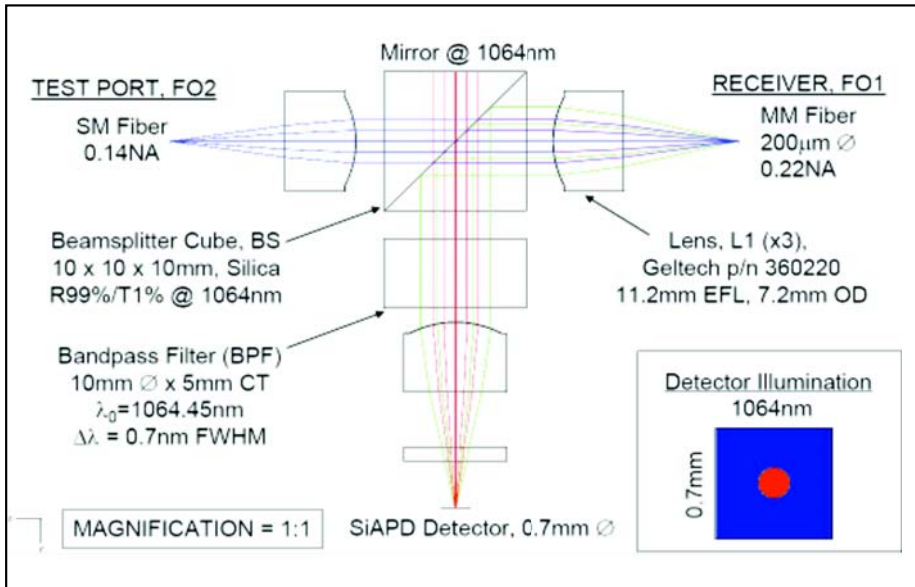
### 3.3 LOLA Receiver and Detector

The LOLA receiver consists of a 14-cm-diameter clear aperture refractive telescope that focuses the received photons on to a fiber optic bundle (FOB). The effective focal length of the telescope is 500 mm. The design and materials of the telescope were chosen to minimize the thermal fluctuations expected on orbit. Since LOLA is not an imaging system, the concern is not to maintain the image quality but to collect the maximum number of photons with the fewest possible losses and to minimize the background radiation. The telescope assembly includes a dielectric fold mirror, which lets all radiation other than 1064 nm pass through and reflects the laser radiation onto the FOB. This minimizes the amount of background solar radiation incident on the detectors. The fiber bundle consists of five identical fibers. Each fiber in the bundle directs the reflected energy into the aft-optics assembly for each detector. The receiver and fiber bundle are shown in Fig. 8.

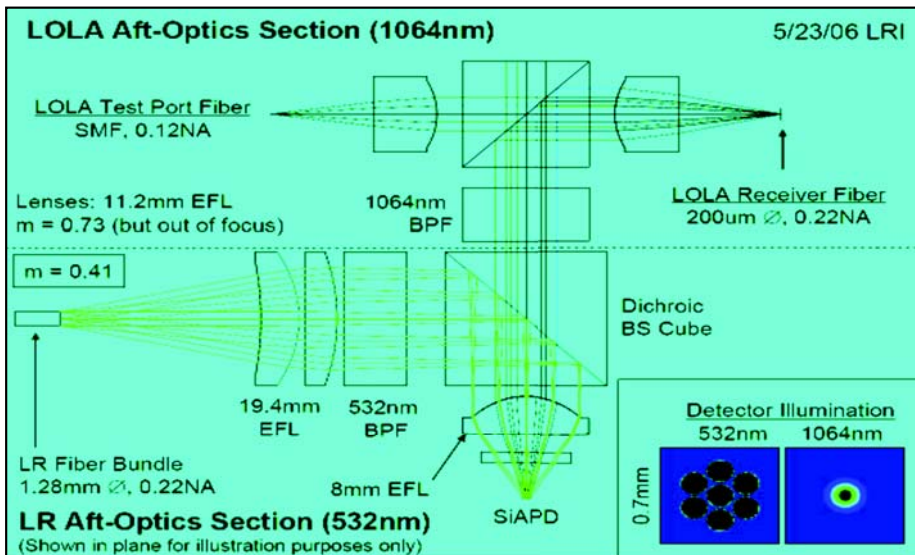
The aft optics assemblies for detectors (channels) 2–5 are identical (Fig. 9). Detector 1 houses the LR aft optics. The aft-optics assembly mounts directly on a flange that is an integral part of the detector housing assembly. The housing assembly or detector plate includes the detector and all the associated electronics. The aft optics consists of collimating and focusing optics to collimate the output of the fiber and send it on to the detector. A band-pass filter tuned to the laser wavelength is also included in the optical train to minimize the background solar radiation. In addition, the aft optics assembly includes a separate test port with an FC connector. The test port is intended for calibration purposes during instrument integration and testing. Signals from optical test sources can be injected into the test port and exercise the signal processing algorithms and electronics of the instrument. It is also possible to back-illuminate the detectors through the test port and monitor the field of view (FOV) and boresight alignment during the integration process.

The LOLA detectors are part of the detector housing assembly. The housing assembly includes the aft optics, the detector hybrid and the LOLA detector board. The detectors and detector board electronics have low noise and sufficient bandwidth to allow detection of the reflected laser pulses from the lunar surface and measure the time of flight (TOF). Each detector has its own independent gain control and threshold setting. The detector hybrids are the same silicon avalanche photodiodes that were used on the Mars Orbiter Laser Altimeter





## LOLA aft-optics detectors 2-5

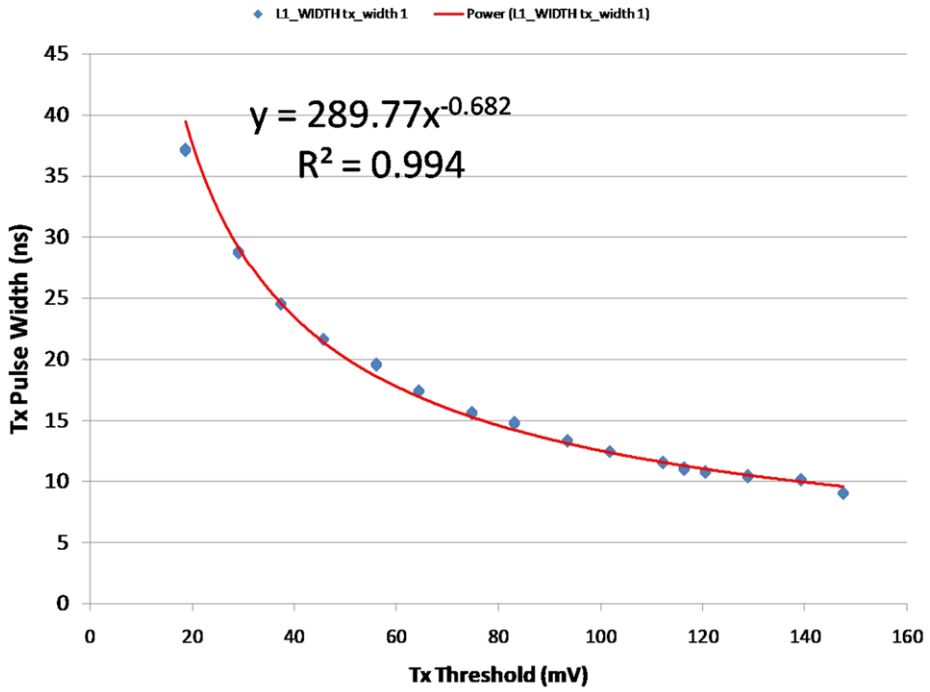


## LOLA aft-optics detector 1

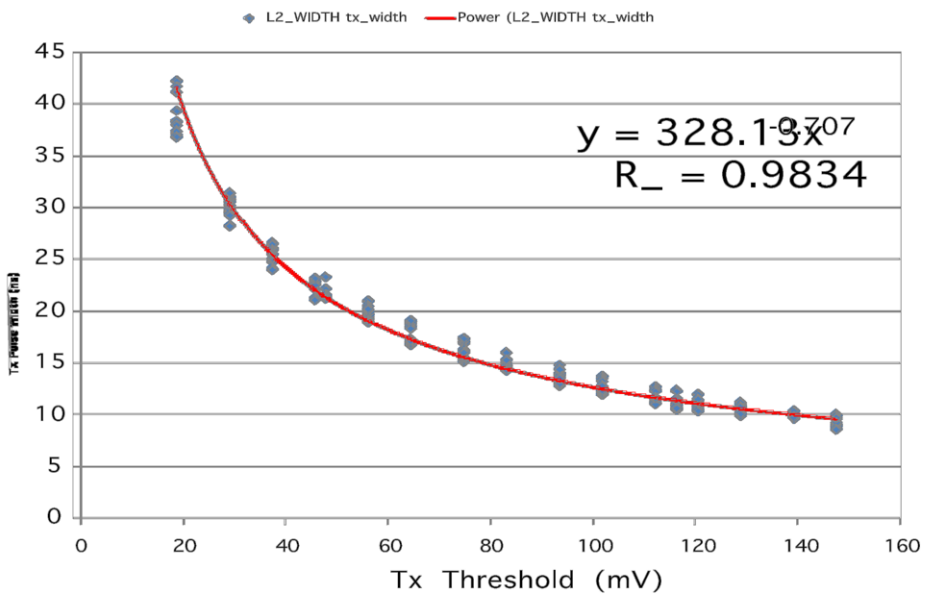
**Fig. 9** Aft optics and test port

(MOLA) (Zuber et al. 1992) and the Geoscience Laser Altimeter (GLAS) (Abshire et al. 2005; Schutz 2001).

The LOLA detector board amplifies the detector hybrid output, and performs two separate functions: a discrimination function to provide timing information to the Digital Unit



Laser 1 Tx pulse threshold sweep



Laser 2 Tx pulse threshold sweep

Fig. 10 Detector thresholds

(DU), and an energy measurement function that integrates and samples the peak of the amplified hybrid output.

The amplification of the hybrid output is performed by a variable gain amplifier (VGA) and a fixed gain buffer with a gain of 5. The VGA gain is variable over a range of  $<0.5$  to 10, controlled by an externally generated d.c. voltage from the DU. The gain control voltage is scaled and level-shifted on the detector board. The discrimination function for the timing information is performed by a high-speed comparator. The threshold level is set by the DU and fed directly to the comparator input.

The energy measurement function is performed by an integrator and a peak detector. It is not dependent on the threshold set by the DU but it is affected by the gain setting. The integrator stage is combined with a track-and-hold function, which is controlled by a latch. The latch is set by a peak detector, and later reset by a signal from the DU. The peak detector responds to the integrator output so as to set the latch at the time of the maximum output from the integrator. The latch then puts the integrator into its HOLD mode until its output is digitized. The peak detector is an a.c.-coupled, d.c. offset constant-fraction discriminator. The output is proportional to the received energy.

### 3.4 LOLA Digital Unit

The LOLA Digital Unit provides two fundamental categories of functionality for the instrument. The first category—range measurement—includes firing the laser and acquiring LR data. The other category—command and telemetry (C&T)—comprises receiving and distributing spacecraft commands, collecting, formatting and transmitting telemetry, as well as monitoring and processing ranging information for real-time control of the altimeter's parameters such as the range gate, amplifier gain and detector threshold.

Two different time measurements are made by the electronics. The primary is the time-stamping of the laser transmit pulse and the five lunar return pulses, and the LR pulse. The timing reference is based on redundant 20 MHz ultra stable oscillators (USO) located in the spacecraft, which is divided to 5 MHz and used as the internal timing reference. The spacecraft provides a non-redundant 1 Hz pulse, which is used to synchronize all LOLA activities. The fault-tolerant design allows for the spacecraft timing signals to replace the function of the internal clock oscillator, while the internal oscillator is sufficient to operate the instrument in the absence of any spacecraft timing reference. Also, circuits will use the spacecraft's USO to measure the frequency of the oscillator, for purposes of calibration and trending.

LOLA's pulse repetition frequency (PRF) of 28 Hz is phase locked to the spacecraft's 1-Hz timing signal. Each 1-s interval is referred to as a major frame, which consists of 28 approximately 35.7 ms periods referred to as a minor frames. The time within a minor frame is allocated for various functions, which include an 8 ms window for receiving the Earth laser signal (LR), a window for receiving the reflections from the Moon, and time for transmitting science and engineering data to the C&T Electronics. The Range Measurement Electronics also synchronizes the operation of the Analog Electronics and controls resetting of the energy measurement circuits for Detector boards.

The Range Measurement Electronics control is implemented in a single RTAX2000S Field Programmable Gate Array (FPGA). This FPGA also contains a variety of counters which implement the 200-ns coarse timer for each channel, noise counters, event counters, and calibration counters for measuring the margin in the digital phase lock loops in each of the twelve fine timing microcircuits. There are six physical channels in the Range Measurement Electronics. One channel is utilized for the timing laser firing pulse, and the other

five are for the lunar return pulses, with one of the return channels also time-shared for the Earth laser time measurement. The time measurement method utilizes a coarse timer implemented in the FPGA along with fine timing supplied by the digital ASIC time-to-digital converter (TDC) originally designed to support the European Space Agency's (ESA's) Automated Transfer Vehicle (ATD). The FPGA and TDC circuits together allow for time-tagging over planetary distances of the time that the laser is fired, the time the Earth-based LR signal arrives at the spacecraft, and the time of each of 5 returns are received from the Moon; the LOLA altimeter has a time resolution of approximately 28 ps.

### 3.5 Laser Transmitter Telescope

The LOLA laser transmitter telescope has two functions: it reduces the divergence of the LOLA laser oscillator input beam, and it splits the output beam into five to generate a cross pattern in the far field. The telescope is an  $18\times$  magnification, afocal, Galilean beam expander that expands and collimates the LOLA Laser 1 mm and 1.8 mrad  $1/e^2$  diameter input beam to generate the required 100  $\mu$ rad  $1/e^2$  diameter output beam divergence. The telescope has a single Corning 7980 fused silica negative lens, a BK7G18 positive lens group. It also contains the DOE that splits the output beam. The DOE optic is a 40-mm diameter by 6-mm thick fused silica substrate etched on one side with a transmission phase grating and anti-reflection (AR) coated on both sides to maximize transmission at 1064 nm. The LOLA DOE was manufactured by MEMS Optical from a master pattern that is replicated via a proprietary lithographic process onto a fused silica wafer from which multiple parts can be cored out. The flight DOE had an overall efficiency of 80% with the center beam having nearly twice the energy of the outer beams.

The telescope tube is beryllium with a titanium flexure pre-loaded to 30 lbs in order to securely hold the positive lenses and DOE over all expected mechanical and thermal loads. The exit optics contain a 36-mm-diameter exit clear aperture. The LOLA assembly is 165 mm long and weighs 120 g, and has an operational thermal range of  $20 \pm 20^\circ\text{C}$ , and a survival thermal range of  $-30^\circ\text{C}$  to  $+70^\circ\text{C}$ . Two flight model (FM) Laser Transmitter Telescopes were integrated, functionally tested in air and vacuum, thermally qualified for survival, and delivered to the LOLA laser team for integration to the Laser Bench. Further details on the transmitter telescope are given in Ramos-Izquierdo et al. (2009).

### 3.6 LOLA Receiver Telescope

The LOLA Receiver Telescope (LRT) has a 150-mm-diameter objective lens and an unfolded path length to provide an  $f/2$  objective lens speed. The LRT opto-mechanical design is a beryllium structure with titanium flexures, tolerances, optic mounting techniques, and alignment compensators for focus and boresight. The receiver FOV is determined by the FOB located at the telescope focal plane. The telescope end of the FOB has five 200- $\mu$ m core diameter, 0.22 NA, multimode, step-index fiber-optics spaced 250  $\mu$ m apart in a cross pattern; these fiber-optics define five 400- $\mu$ rad diameter FOV's with a center-to-center spacing of 500  $\mu$ rad. The FOB telescope connector is clocked  $26^\circ$  to align the five receiver FOV's with the five transmitted laser beams. Behind the telescope connector the FOB fans out into five independent fiber-optic cables that attach to the five Aft-Optics/Detector Assemblies. The LOLA receiver system FOV was selected to provide sufficient boresight alignment margin for each laser/receiver pair while having enough angular distance between neighboring channels to prevent crosstalk. Further details regarding the LRT are given in Ramos-Izquierdo et al. (2009).

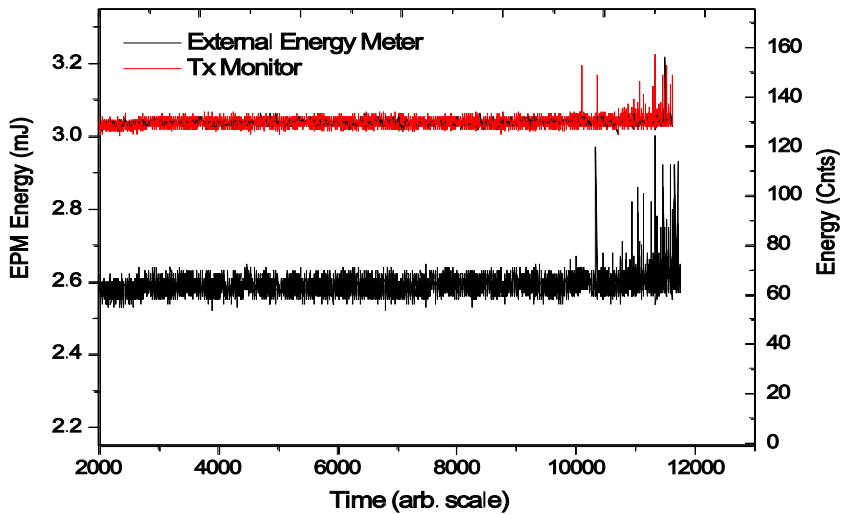


**Fig. 11** Pulse energy calibration

## 4 System Calibration

### 4.1 Transmitter Energy Calibration

The LOLA transmitter has an on-board laser energy sensor (detector), which also serves as the fire acquisition detector. The detector is commonly referred as the SPOT4 or Transmit energy (*Tx* Energy) monitor. The *Tx* Energy monitor was correlated with measurements made with an external energy meter to assess its performance during pre-launch system-level testing (Fig. 11).

By correlating and normalizing the *Tx* Energy monitor with the external energy monitor it is possible to measure the transmitted energy with approximately 1.3% accuracy. There was no degradation in the performance of the *Tx* Energy monitor as a function of temperature. Using data for Laser 1 in the hot and cold plateaus we determined that in the hot case the accuracy was 0.5–1% and in the cold case it was approximately 1.0%. Thus, we can expect the *Tx* energy accuracy requirement of 2% to be met at all temperatures.

The equation that converts *Tx* Energy monitor from counts to laser energy is (Riris et al. 2008)

$$\text{Energy(mjoules)} \approx 0.0207 \times (Tx \text{ Energy(counts)} - 12(\text{counts})). \quad (1)$$

The equation was obtained using ambient data (where the full energy of the laser beam could be measured) and it is an average approximation from different data sets.

The responsivity of the *Tx* Energy monitor changes significantly as function of temperature, therefore a temperature correction must be applied to (1). The temperature correction was derived from the breadboard laser test data and the EM laser TVAC data, where a stable external monitor was present, and it is

$$E(T) = E(T_0) \times [0.82702 \times e^{0.0081816 \times T}], \quad (2)$$

where  $T_0$  is the energy at room temperature ( $T_{\text{room}} = 23.2^\circ\text{C}$ ). There is no temperature sensor on the SPOT4 detector itself. However, the detector should follow the laser bench temperature and the laser electronics assembly (with some lag). It does not get as cold as the laser



bench temperature or as hot as the laser electronics. The average of the two temperatures should be a good indicator of the SPOT4 temperature.

#### 4.2 Receiver Energy Calibration

Each LOLA detector has an energy monitor circuit that estimates the received energy ( $R_x$  Energy) incident on each detector. The received energy per pulse is a direct measure of the lunar surface reflectivity and is given by Gardner (1982)

$$E_{Rx} = E_{Tx} \times \varepsilon_{Rx} \times \frac{A_{Rx} \times \rho}{\pi \times r^2} \quad (3)$$

where  $E_{Rx}$  is the received energy,  $E_{Tx}$  is the transmitter energy,  $\varepsilon_{Rx}$  is the efficiency of the receiver optics (from the telescope to the detector active area),  $A_{Rx}$  is the receiver aperture area,  $\rho$  is the surface reflectivity and  $r$  is the range to the target (lunar surface). By normalizing the received energy to the transmitter energy and knowing the range, we can determine the surface reflectivity of the lunar surface.

The energy monitor is essentially a peak sample and hold circuit with an integrator. Its circuitry is after the variable gain amplifier (VGA) and voltage buffer but before the timing circuit which means it is affected only by the gain setting but not the threshold setting. The circuit is optimized for detection of energies from 0.1 to 3.0 fJ.

The specification for the energy monitor precision is to measure the relative energy within 12% from 0.1 to 3.0 fJ. This specification is met for energies above 0.2 fJ. At 0.1 fJ the precision will can be as large as 30% depending on the detector and temperature. The impact on ice detection has been modeled and its impact should be minimal.

#### 4.3 Counts to Energy Calibration

The energy monitor was characterized at subsystem testing and system-level integration. The energy monitor is to a first approximation, linear with energy, but has a gain-dependent slope and offset. The following equations can be used to convert counts to energy,  $E$ , (in fJ)

$$E = slope(G) \times Counts + offset(G) \quad (4)$$

where,  $slope(G)$  and  $offset(G)$  are the gain-dependent slope and offset. The equation that describes the gain dependent slope is given by

$$slope(G) = A + B \times e^{-\frac{Gain}{\varepsilon}} \quad (5)$$

The offset is best described by a quadratic fit, although a linear fit also gives adequate results:

$$offset(G) = A + B \times Gain + C \times Gain^2 \quad (6)$$

In the above equations  $Gain$  is the gain read back.

Table 3 gives the coefficient values for all 5 detectors. These equations are valid for energies  $\geq 0.2$  fJ. At 0.1 fJ the equations do not give an accurate energy value. Note that *absolute* energy accuracy of  $R_x$  energy monitor (i.e. the counts to fJ conversion) is no better than 20–30%. However, the *relative* energy values (in counts) will remain within the specification of 12% except at the lower energies (0.1 fJ) as indicated in Table 4.

**Table 3** Laser output beam properties

	Laser 1 ( $\mu\text{rad}$ )	Circularity	Laser 2 ( $\mu\text{rad}$ )	Circularity
Ambient 1 Atm	153.1	Out of focus	147.9	Out of focus
Ambient 0 Atm (Start)	100.0	1.08	94.9	1.19
Hot Qual.	106.7	0.96	97.5	1.18
Cold Qual./Op.	103.6	1.30	110.7	1.24
Hot Operational	104.5	1.29	102.5	1.17
Ambient 0 Atm (End)	109.9	1.14	101.7	1.30

**Table 4** Energy monitor counts to energy calibration

	Slope coefficients			Offset coefficients		
	A	B	C	A	B	C
Detector 1	0.00914	0.07437	13.4092	-0.84429	0.03313	-0.00032235
Detector 2	0.00829	0.07399	12.9082	-0.82769	0.03376	-0.00034980
Detector 3	0.01103	0.0813	11.44682	-0.63522	0.02518	-0.00025046
Detector 4	0.00985	0.08125	11.10461	-0.8598	0.03452	-0.00033139
Detector 5	0.00852	0.06865	14.19706	-0.74418	0.02174	-0.00010699

#### 4.4 Transmitter Calibration

The laser far field pattern was measured at the subsystem (laser) level with a 4-m focal length off-axis parabola collimator and a charge-coupled device CCD camera at the focal point. The data were analyzed using commercial beam analysis software (BeamView<sup>®</sup> by Coherent). The laser beam profiles after the beam expander integration are shown in Fig. 12.

The laser divergence prior to the beam expander integration was (Riris et al. 2008):

##### *Laser 1*

FF Divergence 1.76 mrad (= 97.8  $\mu\text{rad}$  after  $\times 18$  beam expander)

99% energy enclosed within aperture diameter of 5.7 mm— $1.6 \times 1/e^2$  dia, or <1% of energy lies outside of  $2 \times 1/e^2$  diam.

Circularity = 0.91

##### *Laser 2*

FF Divergence 1.72 mrad (= 95.6  $\mu\text{rad}$  after  $\times 18$  beam expander)

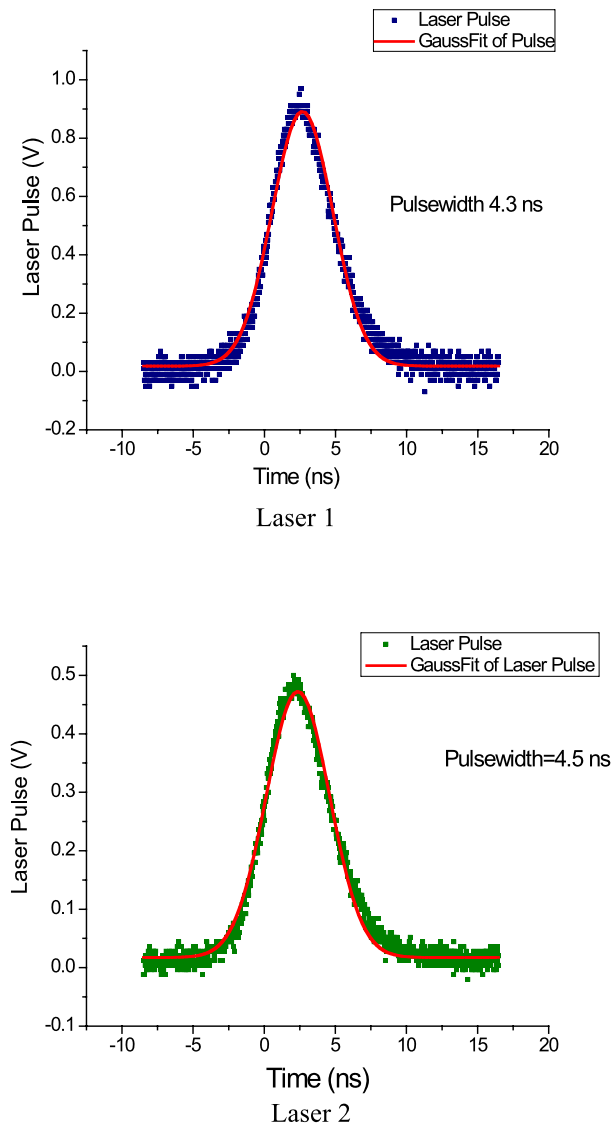
99% energy enclosed within aperture diameter of 5.7 mm— $1.7 \times 1/e^2$  dia, or <1% of energy lies outside of  $2 \times 1/e^2$  diam.

Circularity = 0.97

During system level environmental testing the laser far field pattern was measured using an off-axis parabola and a different CCD camera. The data were analyzed using custom-developed software that fit the laser images to a two-dimensional Gaussian surface. Sample of laser images (along with reference cube images and a fiduciary image) are shown in Fig. 13.

The laser far field pattern remained nearly in the fundamental or TEM<sub>00</sub> mode over the entire operating temperature range. The divergence was calculated as the average of the  $x$

**Fig. 12** Laser transmitter profiles showing transmit pulse shape

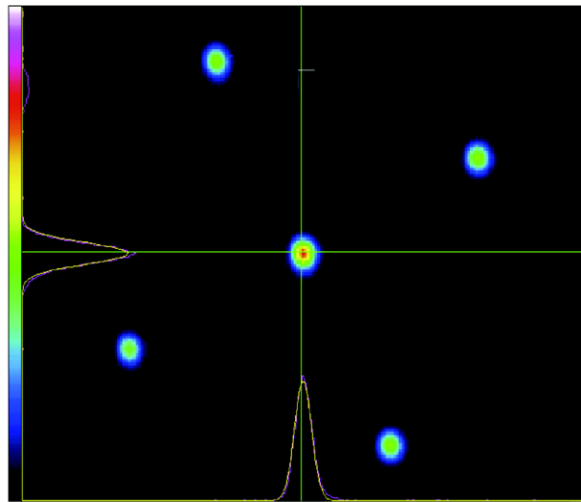


and  $y$  Gaussian  $1/e^2$  widths. The laser divergence and circularity (defined as the ratio of major to minor axes, in this case, the ratio of the  $x$  and  $y$  Gaussian widths obtained by the fit) as a function of temperature are shown in Table 3. Note that at ambient pressure the transmitter optics is out of focus, which results in high divergence.

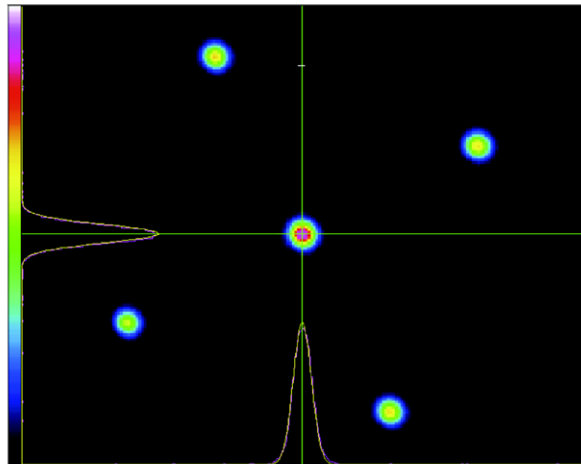
#### 4.5 Laser Pointing Jitter

The laser pointing jitter was monitored at the subsystem level and also during the system level environmental testing. Figure 14 shows the Laser 1 pointing jitter after analyzing 450 images taken under vacuum and at ambient temperature over all temperatures. The images were analyzed for the relative separation between the central laser spot and a reference

**Fig. 13** Laser far field beam patterns showing 5 spots and energy profiles. The center spot has slightly more energy than the outer 4 spots



Laser 1 profile with CCD at simulated vacuum  
Focus (18 mm from OAP focal plane)



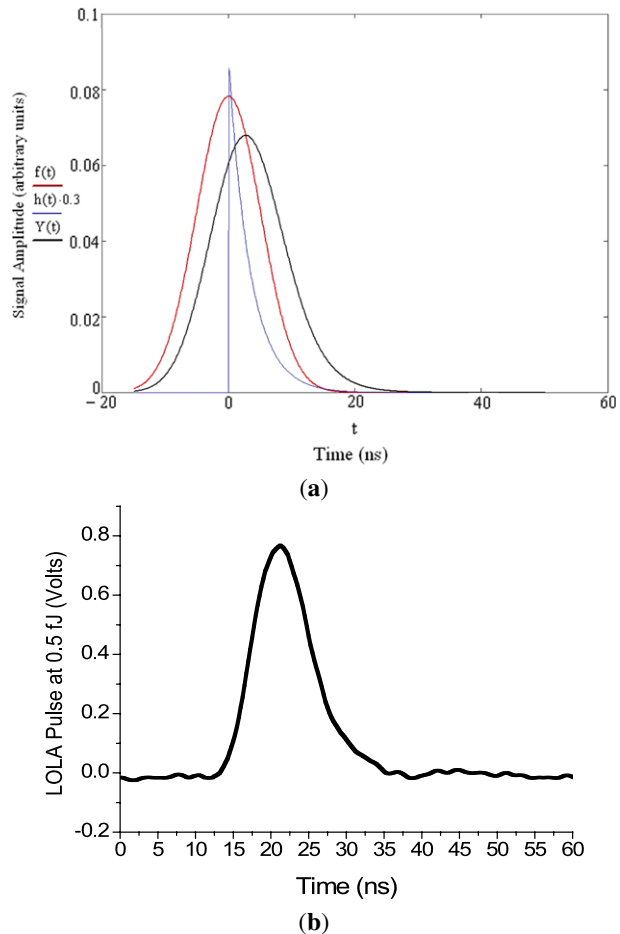
Laser 2 profile with CCD at simulated vacuum Focus  
(18 mm from OAP focal plane)

cube. The jitter in both subsystem and system level environmental testing was approximately 5 mrad in the  $x$  and  $y$  directions (Fig. 15).

#### 4.6 Laser Wavelength

The laser wavelength at the subsystem delivery was 1064.4 nm. During system-level environmental testing the laser wavelength was monitored by a wavemeter (operating in continuous wave—CW—mode). The overall change in the laser wavelength was  $\sim 0.1$ – $0.13$  nm. Discontinuous changes in the laser wavelength were 0.04–0.05 nm. To first order the change

**Fig. 14** (a) Convolution of Gaussian pulse with exponential delay function. (b) LOLA pulse at the output of the VGA



in wavelength (without the discontinuous changes) was  $\sim 0.06\text{--}0.07\text{ nm/}^\circ\text{C}$ . The discontinuous changes in the wavelength could be attributed to changes in the mode structure of the laser and/or the wavemeter operation, which will report the wavelength of only one mode.

#### 4.7 Laser Pulse Shape and Mode-Beating

The laser pulse shape was measured at subsystem (laser) integration using a high-speed photo detector and oscilloscope and during system environmental testing. Sample waveforms from the system level environmental tests are shown in Fig. 12. The pulse width varies from 4.3 to 4.9 ns full width at half maximum (FWHM) amplitude.

The LOLA laser is not a single mode laser. It will occasionally operate in more than one mode and those modes may beat against each other producing a series of very short pulses (shown in Fig. 16 as seen by a high speed photo detector and a fast oscilloscope). The impulse response of the transmit energy monitor will “smear out” the short mode-beating pulses. However, when the laser mode beats there will be an impact on the time of flight (range) measurement. Laser 1 rarely exhibits multi-mode behavior (1–2% of the total number of shots in steady state), whereas Laser 2 exhibits multi-mode behavior much more



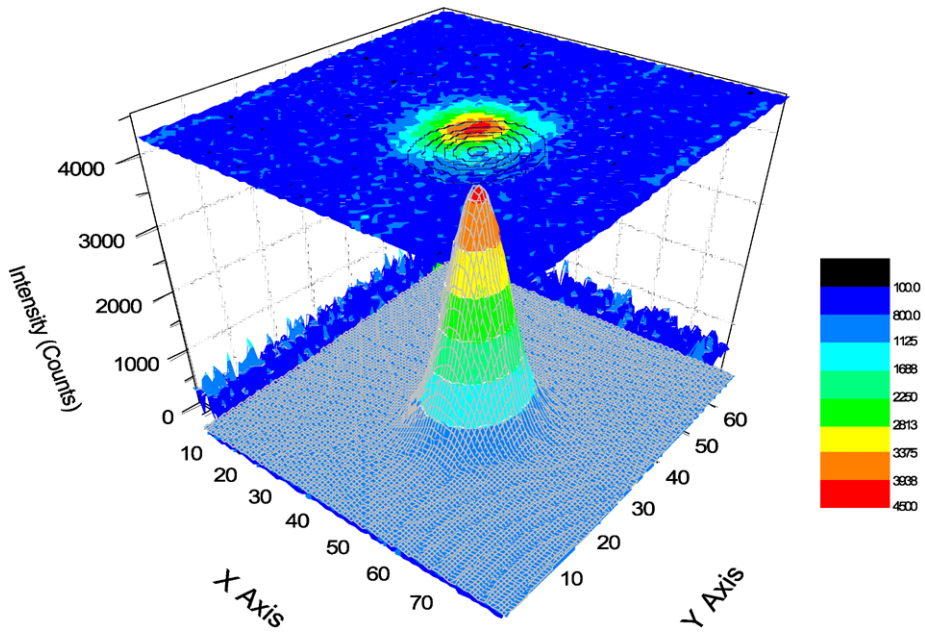


**Fig. 15** Spatial pattern of pulse energy

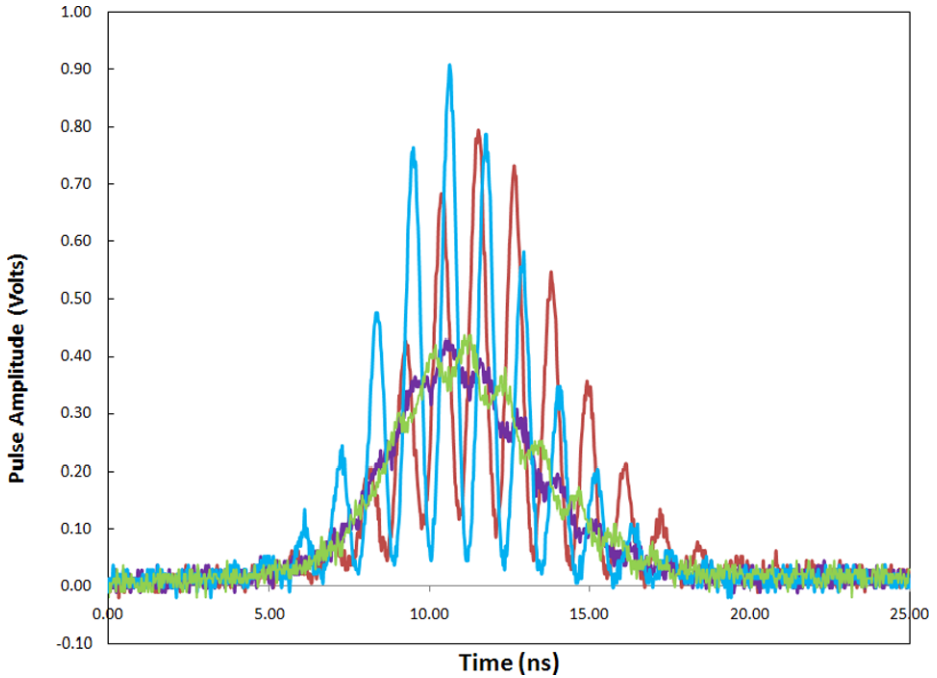


**Fig. 16** Examples of laser mode beating. Mode beating is observed occasionally in laser 1 and more frequently in laser 2

frequently (about 5–25% of the total number of shots) depending on the temperature. The  $T_x$  Energy monitor can be used to detect the multi-mode behavior of the laser since the peak energy shows a large increase. The multi-mode behavior of the laser will impact the time of flight calculation since the transmit pulse will be distorted. However, the  $T_x$  Energy monitor can be used to flag and filter the returns that show multi-mode behavior. An approximate correction can be applied which will be some fraction of the pulse width.

#### 4.8 LOLA Ranging (TOF) Calibration

The primary function of LOLA is to provide time of flight (TOF) or altimetry measurements of the laser pulse which, along with the spacecraft position, can be used for determining the topography of the lunar surface. The LOLA TOF is determined by the following measurements: the  $T_x$  laser pulse leading edge time stamp ( $LET_x$ ), the  $T_x$  laser pulse trailing edge time stamp ( $TET_x$ ), the  $R_x$  laser pulse leading edge time stamp ( $LER_x$ ), the  $R_x$  laser pulse trailing edge time stamp ( $TER_x$ ). The distance from the LRO spacecraft to the illuminated spot on the lunar surface,  $D$ , is related to the laser-pulse TOF by:

$$D = \frac{c}{2} \times (T_x - R_x) \quad (7)$$

where  $c$  is the speed of light in vacuum, and  $T_x$  and  $R_x$  are the times of the transmitted and echo laser-pulses. If the pulse shapes were perfectly symmetric, the pulse arrival times are simply taken as the average value of the signal threshold crossing times at the leading and trailing edges, or

$$T_x = \frac{1}{2} \times (LET_x + TET_x) \quad (8)$$

and

$$R_x = \frac{1}{2} \times (LER_x + TER_x). \quad (9)$$

The distance traveled by the laser-pulse and the spacecraft orbit position and pointing angle at the moment the laser-pulse was transmitted defines a vector in space, which can be used to solve for the coordinates and the height of the laser footprint on the planet surface given the position of the planet center of mass. A topographic map of the planet can be constructed with a great number of such measurements along different ground tracks. For a perfectly symmetric Gaussian pulse waveform, the leading and trailing edge points also provide a measurement of the  $T_x$  and  $R_x$  pulsewidth.

##### 4.8.1 LOLA TOF to Range

In an ideal altimeter where the pulses are perfectly symmetric there would also be no inherent biases in the time of flight. Of course, LOLA is not an ideal altimeter and we need to correct for several biases which are different for each detector. These corrections can be divided in three broad categories. The electronics TOF bias (TDC trailing edge bias), mainly the time to digital converter biases for each channel, the impulse response bias which makes the pulses asymmetric and introduces a range bias (or “time walk”) that is a function of the received signal amplitude and finally fiber delays due to the different fiber lengths for each channel. The range is also reference to a physical point on the instrument (zero range bias).

These corrections will be refined on orbit.

**Table 5** TDC bias

	Phase A		Phase B	
	Average (ns)	Stdev (ns)	Average (ns)	Stdev (ns)
tx	2.22	0.21	1.83	0.15
rx1	1.83	0.18	1.71	0.21
rx2	1.89	0.18	1.83	0.18
rx3	1.77	0.18	1.38	0.18
rx4	1.56	0.18	1.5	0.21
rx5	1.86	0.18	2.04	0.15

#### 4.8.2 TDC Trailing EdgeTime Bias

Each TDC in the digital unit has its own time delay and bias. The trailing edge biases for each TDC were measured during subsystem testing and are listed in the Table 5. The TDC trailing edge biases varied very little over temperature.

The trailing edge bias for each TDC can then be accounted for when computing the midpoint for each pulse using the equations below

$$T_{x_i} = \frac{1}{2} \times [LET_{x_i} + (TET_{x_i} - TDC\ Bias_i)] \quad (10)$$

and

$$R_{x_i} = \frac{1}{2} \times [LER_{x_i} + (TER_{x_i} - TDC\ Bias_i)] \quad (11)$$

where  $i = 1, 2, 3, 4, 5$  for each channel/detector.

#### 4.8.3 Pulswidth and Impulse Response Bias

The impulse response of the detectors may be modeled, to first order, by a simple RC low-pass filter. The convolution of a Gaussian pulse with the impulse response of an RC low pass filter is the error function. Figure 14a shows a simulation of a Gaussian pulse (red trace) with the impulse response of an exponential decay function from an RC filter (blue trace) and the resulting convolution (black trace) and Fig. 14b shows an actual pulse from the LOLA detector from subsystem testing. The impulse response of the detector will smear out any high frequency components in the laser pulse resulting in slightly wider pulswidth and a “time-walk” as the energy and pulswidth increase.

Since LOLA does not use a constant fraction discriminator it is necessary to correct for this “time-walk”, which is dependent on the gain, threshold, and return pulse energy. For a perfectly symmetric pulse the “time-walk” could have been compensated for by taking the mid-point of the pulse. The “time-walk” correction due to the impulse response of all channels may be modeled in three different ways:

1. A simple exponential (a lowpass RC filter with  $R = 50\ \Omega$  and  $C = 68\ \text{pF}$ ).
2. A single-pole butterworth filter based on the actual frequency response of the subsystem testing (cf. Riris et al. 2008).
3. An empirical formula derived from test data that accounts for the pulse broadening and “time walk” effect based on the gain and threshold readback and the received energy.

**Table 6** Minimum detectable energy (in counts) in each LOLA detector

Detector 1	12
Detector 2	13
Detector 3	10
Detector 4	13
Detector 5	13

We are currently investigating and modeling all 3 options. At this time we have preliminary results for the third method which seems to yield the satisfactory results and is the one we will present in this paper. The final time-walk corrections will be presented in the final calibration report to the LRO Project and will be verified on orbit.

In order to account for the different thresholds, gains and energies we form a new variable:

$$x \equiv \frac{\left( \frac{\text{Threshold Readback}}{\text{Gain Readback}} \right)}{\text{Energy} - \text{Energy}_{\min}} \quad (12)$$

where,  $\text{Energy}$  is the energy in counts and  $\text{Energy}_{\min}$  is the minimum energy (in counts) for each channel, which is listed in Table 6. Then the range offset due to the time walk correction is given by

$$\begin{aligned} \text{Range\_Offset} = & \text{slope\_n}(\text{gain\_readback}) * \ln(\text{Threshold Readback}/\text{energy}) \\ & + \text{offset\_n}(\text{gain\_readback}). \end{aligned} \quad (13)$$

Using the following polynomials

Slopes

$$\begin{aligned} \text{slope1} &= -0.0009x^2 + 0.0605x - 1.8952, \\ \text{slope2} &= -0.0008x^2 + 0.05x - 1.5695, \\ \text{slope3} &= -0.0007x^2 + 0.0442x - 1.5382, \\ \text{slope4} &= -0.0008x^2 + 0.0548x - 1.6802, \\ \text{slope5} &= -0.0008x^2 + 0.051x - 1.7203. \end{aligned}$$

Offsets

$$\begin{aligned} \text{offset1} &= -8E-05x^3 + 0.0053x^2 - 0.0945x + 4.770, \\ \text{offset2} &= -1E-04x^3 + 0.0067x^2 - 0.1449x + 4.277, \\ \text{offset3} &= -7E-05x^3 + 0.0047x^2 - 0.1124x + 3.135, \\ \text{offset4} &= -9E-05x^3 + 0.006x^2 - 0.1158x + 0.000, \\ \text{offset5} &= -3E-05x^3 + 0.0012x^2 - 0.0133x + 1.120. \end{aligned}$$

If  $\text{Energy} - \text{Energy}_{\min} = 0$ , then only the constant term in  $\text{offset\_n}$  above is used.

**Table 7** LOLA detector timing biases

Detector 1 (ns)	Detector 2 (ns)	Detector 3 (ns)	Detector 4 (ns)	Detector 5 (ns)
$10.9236 \pm 0.227$	$9.4533 \pm 0.226$	$8.1327 \pm 0.289$	$5.3142 \pm 0.369$	$7.221 \pm 0.240$

#### 4.8.4 Fiber Time Bias and Zero Reference (Zero Range)

The range offset bias due to the different length of the fiber optic cables in the 5 channels was measured at the system level. Table 7 gives the timing bias for each channel. The range bias is referenced to the front of the LOLA receiver. It can also be referenced to the LOLA cube. The distance between the LOLA receiver and the LOLA reference cube is 15.174 cm.

## 5 Observation Strategy

In terms of coverage, LOLA will under sample the lunar surface in cross-track coverage and for this reason the basic observational strategy is to operate continuously and obtain as much coverage of the Moon as is possible within operational constraints. Further, the instrument is a nadir-viewing and therefore primarily acquires observations along the spacecraft ground track and provides the “landing strip” information described earlier. However, certain exploration and science investigations can require LOLA observations away from the ground track and therefore LOLA is required to operate off-nadir. Off-nadir observations are possible with LOLA and other laser altimeters. Notably, MOLA (Zuber et al. 1992) at Mars and MLA (Cavanaugh et al. 2007) at Mercury, have both obtained off-nadir observations; MOLA on a regular basis as the MGS spacecraft changed attitude to enable the imaging system to acquire specific targets (Smith et al. 2001), and MLA during two flybys in which the emission angle exceeded  $60^\circ$  (Zuber et al. 2008b).

The observation of potential landing sites and special locations, such as inside permanently shadowed regions (where LOLA is one of the few instruments capable of making observations), may require dense observations with coverage as uniform as possible. Off-nadir pointing by only 1 or 2 mrad from 50-km altitude can move the LOLA swath on the surface by 50 or 100 m and thereby improve the distribution of LOLA tracks across a region.

## 6 Data Analysis, Interpretation, and Modeling

### 6.1 LOLA Data

LOLA data packets consist of time-ordered, round-trip, time-of-flight ranges to the lunar surface, preceded by housekeeping and ancillary data. These 3424-byte packets are output over the spacecraft IEEE-1553 data bus at 1-s intervals and aggregated into  $\sim 1$  megabyte-sized files on the LRO Solid State Recorder. The raw, uncalibrated data comprise the experiment data record (EDR) product. After range calibration and orbital processing, the position of each laser spot is located on the surface using a spacecraft trajectory, attitude history, and a lunar orientation model. The reduced data records (RDR) contain calibrated, geolocated pulse returns, altitudes and reflectivities. Higher-level gridded and transformed data products are produced from the cumulative RDR product.



The LOLA science data from each downlink tracking pass will be aggregated by the LRO Ground Data System and transmitted daily to the GSFC LOLA Science Operations Center (SOC) computer, together with spacecraft event, housekeeping and attitude data. The raw Deep Space Network (DSN), Universal Space Network (USN), and White Sands 1 (WS1) tracking data and supporting products will also be forwarded to the SOC. Each EDR file, ~300 per day, is processed in a pipeline. The geolocation processing cycle will collect the data records into half-orbits, 25–26 per day, with manageable file sizes (~25 megabyte per product). The northern half-orbit begins at the spacecraft ascending node and the southern half-orbit begins at the descending node, following the LRO Project orbital numbering convention.

The timing of LOLA instrument events is derived from the LRO USO, which is monitored by ground stations. Time systems aboard LRO employ Coordinated Universal Time (UTC) to correlate spacecraft Mission Elapsed Time (MET) to ground time with an accuracy of  $\pm 3$  ms. The correlation of MET time to Barycentric Dynamical Time (TDB) is maintained at much higher precision by the LR system and orbital theories. The LOLA data analysis uses TDB as its primary time system (see <http://tycho.usno.navy.mil/systime.html> for details regarding the difference). Spacecraft states relative to the Solar System Barycenter (SSB) at the laser transmit and detector receive times are projected along the instrument boresight and return path vectors to match the observed time of flight, correcting for the aberration of light and general-relativistic time delays. SSB states are determined in the Earth Mean Equator of 2000 (J2000) inertial reference frame using lunar spacecraft trajectories and the DE421 planetary ephemeris (Folkner and Williams 2008). The speed of light is applied to the boresight time-of-flight to locate the laser bounce point in barycentric coordinates. The bounce points are transformed to a selenodetic coordinate frame about the center of mass of the Moon using the DE421 Moon Mean-Earth and Rotation Pole (MOON\_ME) lunar orientation model. The DE421 model incorporates 37 years of Lunar Laser Ranging (LLR) data, thereby providing the geodetic framework for LOLA. The lunar radius and position are then subjected to orbital crossover analysis (Neumann et al. 2001; Rowlands et al. 1999) to minimize the terrain mismatch at the intersections of ground tracks. Empirical adjustment of short-term pointing biases is combined with orbital estimation from tracking data to bring the ground tracks into agreement, and produce a dynamically-consistent, geodetically-precise lunar coordinate framework, as well as an improved lunar potential solution, as discussed earlier. The crossover adjustment is performed at monthly intervals following the propulsive orbital adjustment maneuvers that disrupt the dynamical orbit solutions.

The cumulative altimetric data are binned and interpolated at appropriate resolution to generate the gridded data record (GDR) products described in the next section. These products are then transformed to Spherical Harmonic Analysis Data Records (SHADR) of shape, time-averaged reflectivity, and related geodetic parameters.

Initial quick-look profiles are generated using orbital and attitude data provided by the GSFC Flight Dynamics Facility, and can be displayed in a web browser. Automated editing flags the noise returns and occasional Earth ranges received by Detector 1. After error checks, labeling, manual inspection of edited products, and registration with images obtained by the co-boresighted LRO cameras (Robinson et al. 2009), the EDR and RDR products are validated for delivery to the Planetary Data System (PDS). Refined altimetry is generated in the course of orbital processing by the GEODYN software system (Pavlis et al. 2001), and is released at quarterly intervals as specified in the LRO-LOLA Data Management and Archive Plan. Releases to the PDS Geosciences Node occur at specific intervals, while the current best solutions are made accessible to LRO scientists via a Data Node of the PDS hosted by the LOLA SOC.

**Table 8** Standard data product sizes and delivery rates

Product	Product size	Production rate	Expected number of products for nominal mission	Expected total data volume for nominal mission
LOLA_EDR	1 MByte	296 per day, average	108000	108 GB
LOLA_RDR	24 MByte	25–26 per day	9400	225 GB
LOLA_GDR	~2 GByte	monthly refinements of ~100 data products	100	200 GB
LOLA SHADR	5 MByte	release at quarterly intervals	4	~1 GB

## 6.2 Quick-Look Data Analysis

A quick-look web-based interface has been developed for near-real-time assessment of LOLA data. Data are displayed for each of the five LOLA profiles, and also for the surface reflectivity and roughness. These data are uncorrected and are not suitable for scientific analysis but together with the global map of data distribution can be used for assessing adequacy of coverage and general functioning of the instrument, and in particular for any missing data or changes in the probability of data return from the lunar surface.

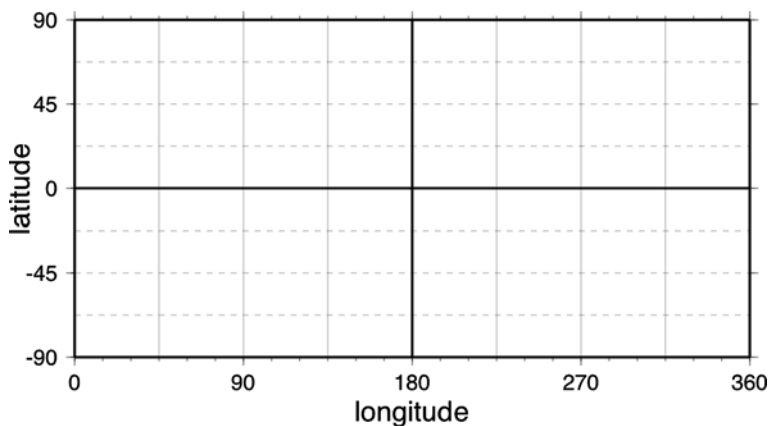
## 7 Science Data Products

Table 8 summarizes expected sizes and production rates for the LOLA Standard Data Products. These products, with detached PDS labels, will be organized into daily and monthly directories. The RDR observations from multiple orbits will be transformed to useful map projections, binned (median-averaged) and interpolated to fill regions lacking data.

A control network for the Moon, consisting of images and control points, will be tied to a topographic reference surface, for which the LOLA GDR is the primary datum. The GDRs are raster Digital Elevation Models of the lunar radius with respect to a spherical datum about the center of mass, and are generated at multiple resolutions (Table 9) as accumulating coverage permits to match the characteristics of image mosaics and other instrument products. Surface slope, roughness, and albedo gridded products will likely be noisier and less amenable to interpolation than altimetry, so will be generated only at a subset of resolutions given in Table 9 unless a specific need arises, in which case special products will be produced. The size of the products at highest resolution may require that they be aggregated in subsets of global coverage. Global products use the equi-rectangular map projection, while the higher-resolution products afforded by dense polar coverage use the Polar Stereographic projection. Tiling will be employed to limit the size of individual products to less than 2 GB to facilitate electronic data transfer. The GDRs are formatted as binary images.

**Table 9** LOLA equi-rectangular map-projected Digital Elevation Models

Product	Product size	Pixel size (m in lat)	Number/size of tiles	Bits per pixel
LDEM_4	4 MByte	7580.8	Global, 0-360	32
LDEM_16	64 MByte	1895	Global, 0-360	32
LDEM_32	256 MByte	947.6	Global, 0-360	32
LDEM_64	1 GByte	473.8	Global, 0-360	32
LDEM_128	2 GByte	236.9	Global, 0-360	16
LDEM_256	4 × 2 GB	118.45	4 tiles, longitudes 0:180:360 by N/S	16
LDEM_512	16 × 2 GB	59.225	16 tiles, longitudes 0:45:90:135:180:225:270:315:360 by N/S	16
LDEM_1024	64 × 2 GB	29.612	64 tiles, longitudes as above, in 22.5° latitude bands	16

**Fig. 17** Equirectangular map projection. Lines show tiling subdivisions of LDEM\_256 (*bold*), LDEM\_512 (*fine*), and LDEM\_1024 (*dashed*)

Binary elevation data may consist of 16-bit integers scaled to a dynamic range of 1728 to 1748 km, or as 32-bit integers scaled to millimeters. The resolution of equi-rectangular pixels will be powers of two pixels per degree of longitude and latitude. The resolution of polar projected pixels will be integral numbers of meters, scaled by a radius of 1737.4 km. Anticipated tiles are shown in Figs. 17 and 18. Where feasible, products may also be provided in a geo-referenced JPEG-2000 format.

## 8 Summary

The LOLA instrument was delivered to the LRO spacecraft in April 2008 and along with the other instruments integrated with the spacecraft. As of January 2009, the LRO spacecraft

**Fig. 18** Polar stereographic map projection from 45N to pole. Circles show outlines of LDEMs at various resolutions. Innermost circles enclose 10- and 5-m DEMs

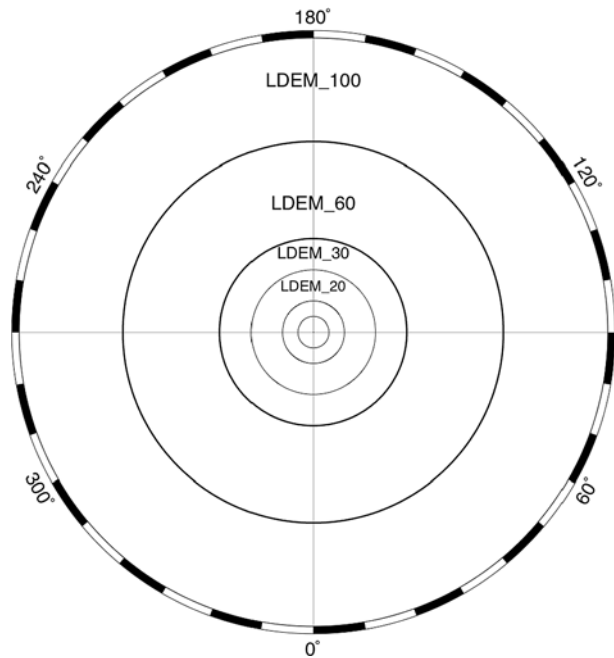


**Table 10** Polar stereographic map-projected Digital Elevation Models

Product	Dimension	Pixel size	Latitude range	Bits/pixel
LDEM_100	28786 × 28786	100 × 100 m	+/-45° to pole	16
LDEM_60	31036 × 31036	60 × 60 m	+/-60° to pole	16
LDEM_30	30496 × 30496	30 × 30 m	+/-75° to pole	16
LDEM_20	30400 × 30400	20 × 20 m	+/-80° to pole	16
LDEM_10	30342 × 30342	10 × 10 m	+/-85° to pole	16
LDEM_5	30328 × 30328	5 × 5 m	+/-87.5° to pole	16

has completed thermal vacuum testing and is being readied for shipment to the launch site. The LOLA instrument is a significant advance in capability over previous planetary laser altimeters because of its multiple beams and laser ranging component, and is expected to contribute a unique dataset for lunar science and exploration.

**Acknowledgements** We are pleased to acknowledge the support and assistance of the LRO Project, particularly the Payload Manager, Arlin Bartels and Project Manager Craig Tooley, without whom the LOLA instrument could not have been built. We also thank the Review Boards that provided sanity and constructive thought during the LOLA development process.

## References

- J.B. Abshire et al., Geoscience Laser Altimeter System (GLAS) in the ICESat mission: On-orbit measurement performance. *Geophys. Res. Lett.* **43**, L21S02 (2005)
- H. Araki et al., Lunar global shape and polar topography derived from Kaguya-LALT laser altimetry. *Science* **323**, 897–900 (2009)

- B.A. Archinal, et al., U.S. Geological Survey Open File Report 2006-1367, 21 pp., 2006. [pubs.usgs.gov/of/2006/1367/](http://pubs.usgs.gov/of/2006/1367/)
- J.F. Cavanaugh et al., The Mercury Laser Altimeter instrument for the MESSENGER mission. *Space Sci. Rev.* **131**, 451–480 (2007)
- G. Chin et al., Lunar Reconnaissance Orbiter overview: The instrument suite and mission. *Space Sci. Rev.* **129**, 391–419 (2007). doi:[10.1007/s11214-007-9153-y](https://doi.org/10.1007/s11214-007-9153-y)
- A.C. Cook et al., Lunar polar topography derived from Clementine stereoisimages. *J. Geophys. Res.* **105**, 12,023–12,033 (2000)
- J.O. Dickey et al., Lunar laser ranging: A continuing legacy of the Apollo program. *Science* **265**, 482–490 (1994)
- W.M. Folkner, J.G. Williams, *Planetary Ephemeris DE421 for Phoenix Navigation* (Jet Propulsion Laboratory, Pasadena, 2008)
- H. Frey et al., Ancient lowlands on Mars. *Geophys. Res. Lett.* **29** (2002). doi:[10.1029/2001GL013832](https://doi.org/10.1029/2001GL013832)
- C.S. Gardner, Target signatures for laser altimeters: an analysis. *Appl. Opt.* **21**, 448–453 (1982)
- S. Goossens, K. Matsumoto, Lunar degree 2 potential Love number determination from satellite tracking data. *Geophys. Res. Lett.* **35** (2008). doi:[10.1029/2007GL031960](https://doi.org/10.1029/2007GL031960)
- W.M. Hartmann, Lunar cratering chronology. *Icarus* **13**, 299–301 (1970)
- W.M. Hartmann, Moon: Origin and evolution of multi-ring basins. *Moon* **3**, 3–78 (1971)
- J.A. Kamalakar et al., Lunar ranging instrument for Chandrayaan-I. *J. Earth Syst. Sci.* **114**, 725–731 (2005)
- A.S. Konopliv et al., Recent gravity models as a result of the Lunar Prospector mission. *Icarus* **150**, 1–18 (2001)
- H.J. Melosh, *Impact Cratering: A Geologic Process* (Oxford University Press, New York, 1989). 245 pp.
- G.A. Neumann et al., The crossover analysis of MOLA altimetric data. *J. Geophys. Res.* **106**, 23,753–23,768 (2001)
- S. Nozette et al., The Clementine mission to the Moon: Scientific overview. *Science* **266**, 1835–1839 (1994)
- D.E. Pavlis et al., GEODYN Operations Manuals. Raytheon ITTS Contractor Report, Lanham, MD, 2001
- H. Qian, Topography of the Moon from the Chang'e Laser Altimetry Data, 2008
- W. Quaide, Rilles, ridges and domes—Clues to maria history. *Icarus* **4**, 374–389 (1965)
- L. Ramos-Izquierdo et al., The Lunar Orbiter Laser Altimeter (LOLA) optical subsystem, 2009
- H. Riris et al., LOLA Calibration Report. NASA/Goddard Space Flight Center, Greenbelt, MD, 2008
- M.S. Robinson et al., The Lunar Reconnaissance Orbiter Camera (LROC). *Space Sci. Rev.* (2009, this issue)
- D.D. Rowlands et al., The use of laser altimetry in the orbit and attitude determination of Mars Global Surveyor. *Geophys. Res. Lett.* **26**, 1191–1194 (1999)
- R.A. Schultz et al., Igneous dikes on Mars revealed by Mars Orbiter Laser Altimeter topography. *Geol. Soc. Am. Bull.* **32**, 889–892 (2004)
- B.E. Schutz, Laser altimetry and LIDAR from ICESat/GLAS. *IEEE Geosci. Remote Sens.* **3**, 1016–1019 (2001)
- D.E. Smith et al., Topography of the Moon from the Clementine LIDAR. *J. Geophys. Res.* **102**, 1591–1611 (1997)
- D.E. Smith et al., The global topography of Mars and implications for surface evolution. *Science* **284**, 1495–1503 (1999)
- D.E. Smith et al., Mars Orbiter Laser Altimeter: Experiment summary after the first year of global mapping of Mars. *J. Geophys. Res.* **106**, 23,689–23,722 (2001)
- L. Soderblom, A model for small-impact erosion applied to the lunar surface. *J. Geophys. Res.* **75**, 2655–2661 (1970)
- P.D. Spudis et al., Ancient multiring basins on the Moon revealed by Clementine laser altimetry. *Science* **266**, 1848–1851 (1994)
- X. Sun et al., Radiometry measurements of Mars at 1064 nm using the Mars Orbiter Laser Altimeter. *EOS Trans. Am. Geophys. Un.* **82**, 2001
- U.S. Geological Survey, Color-coded topography and shaded relief map of the lunar near side and far side hemispheres. Flagstaff, AZ, 2002, pp. I-2769
- M.A. Wieczorek, Gravity and topography of the terrestrial planets. *Treatise Geophys.* **10**, 165–206 (2007)
- M.T. Zuber et al., The Mars Observer Laser Altimeter investigation. *J. Geophys. Res.* **97**, 7781–7797 (1992)
- M.T. Zuber et al., The shape and internal structure of the Moon from the Clementine mission. *Science* **266**, 1839–1843 (1994)
- M.T. Zuber et al., Outstanding questions on the internal structure and thermal evolution of the Moon and future prospects from the GRAIL mission. *Lunar Planet. Sci. Conf.* **XXXIX**, #1074 (2008a)
- M.T. Zuber et al., Laser altimeter observations from MESSENGER's first Mercury flyby. *Science* **321**, 77–79 (2008b)
- M.T. Zuber et al., The Lunar Reconnaissance Orbiter laser ranging investigation. *Space Sci. Rev.* (2009, this issue)